Dalton Transactions

Accepted Manuscript

ROYAL SOCIETY OF CHEMISTRY

www.rsc.org/dalton

Journal Name

RSCPublishing

ARTICLE

Syntheses, Structures and Properties of 5-Azotetrazolyl Salicylic Acid and Its Dilanthanide Complexes

Cite this: DOI: 10.1039/x0xx00000x

Received 00th January 2012,
Accepted 00th January 2012

DOI: 10.1039/x0xx00000x

www.rsc.org/

Wen-Bin Chen,[a] Zhi-Xin Li,[a] Xin-Wei Yu,[a] Meng Yang,[a] Yan-Xuan Qiu,[a] Wen Dong,*[,a] and Ya-Qiu Sun*[,b]

Two hydrated 5-azotetrazolyl salicylic acid (H_3ASA) of [(H_3ASA)·H_2O] (**1**) and [(H_3ASA)·$4H_2O$] (**2**) and five H_3ASA based dinuclear Ln^{3+} complexes of {[$Ln_2(H_{1.5}ASA)_4(H_2O)_8$]·$6H_2O$} [Ln = Dy (**3**), Tb(**4**)], {[$Gd_2(H_{1.5}ASA)_4(H_2O)_8$]·$5H_2O$} (**5**), {[$Sm_2(H_{1.5}ASA)_4(H_2O)_8$]·$6H_2O$} (**6**) and {[$Eu_4(H_{1.5}ASA)_8(H_2O)_{18}$]·$10H_2O$} (**7**) have been synthesized and characterized by single crystal X-ray diffraction analysis. In **1** and **2**, the neutral H_3ASA molecules show a trans-enol-E isomer but display two different dihedral angles. Complexes of **3**-**7** exhibit three types of dinuclear structures in which the anionic ligands show two trans-enol-E/Z isomers. The photochromic and photoluminescent properties for **1**, **3**-**7** and the magnetic properties for **3**-**7** were investigated.

Introduction

In the past decades, a great deal of research has been carried out on lanthanide complex-based inorganic–organic hybrid materials due to their multifunctional, versatile and modulated properties.[1] It has been believed that the types of hybrid materials can not only preserve or even improve the respective features of the components but also produce new properties depending on the synergy between the organic ligands and inorganic lanthanide ions. Because of intrinsic abundant photoluminescent and magnetic properties of lanthanide ions, the inorganic–organic hybrid lanthanide complexes can exhibit potential applications in the development of new luminescent and magnetic materials.[2] Currently, it is a particular challenge to assemble the novel lanthanide complexes with different functional properties.[3] An efficient approach for generation of hybrids is to assemble appropriate organic ligands into lanthanide ion systems by coordinating bonding interactions. Because different ligands can control the structures and properties of the target molecules by different coordinating and bridging modes, choosing the right ligands show particularly important for synthetic strategy. Triazole, tetrazole and salicylic acid have been proven to date desirable ligands due to their multicoordinating atoms and themselves functional properties.4 Meanwhile, azo conjugated aromatic compounds are also desirable types of ligands because azo linker is known to be an efficient electronic bridge, which prompts the creation of extended-conjugated systems, and such types of compounds can show a potential trans to cis photoisomerization property.[5] Very recently, the pronounced bathochromic absorption and photochromism of 1,1'–azobis-1,2,3–triazole, 1,1'–azobis-tetrazole and 5,5'–azotetrazolate based complexes were reported.[6] The H_3ASA, which contains azo, salicylic acid and tetrazole moieties, should be one of especially desirable candidates because it can dissociate mono-, di- and tri-valent anions, and each anion can not only give multiply coordinating and bridging modes, but also exhibit different trans/cis-enol/keto-Z/E isomers based on photoisomerization reactions (Scheme 1). Up to now, the report concerning the structures, photochromic, photoluminescent and magnetic properties of well-defined single crystals of the H_3ASA based Ln^{3+} metallic complexes, to our knowledge, have not been found.[7] Here, seven novel H_3ASA based compounds of **1**-**7** were synthesized and their crystal structures, photochromism, photoluminescence and magnetism were investigated and discussed.

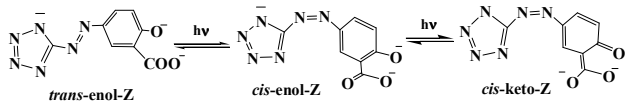

Scheme 1. The photoisomerization reaction ASA^{3-} anion.

Experimental

Materials and Physical Measurements

All the commercial reagents and solvents were used without further purification unless otherwise stated. IR spectra were recorded as pressed KBr pellets on a Bruker Tensor 27 spectrophotometer. Elemental analyses were carried out using a Perkin-Elmer analyzer model 240. UV-vis absorption spectra of **1** in aqueous solution were collected on U-1800 Ultraviolet-Visible Spectrophotometer. The Solid-state diffuse reflectance spectra were measured on a Hitachi UV-2501PC spectrophotometer equipped with an integrating sphere attachment and against a $BaSO_4$ plate as the standard. Luminescence spectra were recorded with an F-4500 fluorescence spectrophotometer. Fluorescent Imaging experiments for solid samples were conducted with Nikon 55i Fluorescent Microscope. The magnetic measurements of the sample of **3**-**7** were carried out using a SQUID magnetometer in the temperature range of 2–300 K at a constant magnetic field (1000 Oe). Ac data were collected in the range 2-5.5 K with an applied alternating field of 3.5 Oe at different frequencies in the range 0-1500 Hz.

X-ray crystallography and data collection

The crystals were filtered from the solution and immediately coated with hydrocarbon oil on the microscope slide. Suitable crystals were mounted on glass fibers with silicone grease and placed in a Bruker Smart APEX(II) area detector using graphite monochromated Mo-Kα radiation (λ = 0.71073 Å) at 173(2)/298(2) K. The structures were solved by direct methods and successive Fourier difference syntheses (SHELXS-97) and refined by full–matrix least-squares procedure on F^2 with anisotropic thermal parameters for all non-hydrogen atoms (SHELXL-97). Hydrogen atoms in the azotetrazolyl were added by electron density peak and other Hydrogen atoms include water hydrogen atoms were added theoretically and were riding on their parent atoms. Crystallographic Data Centre under reference numbers CCDC 922441 for **1**, 946733 for **2**, 922442 for **3**, 922443 for **4**, 922444 for **5**, 922445 for **6**, 922446 for **7**.

Quantum Calculations

All the quantum-chemical calculations were done with the Gaussian 09 suite by the time dependent density functional theory (TD-DFT) method at B3LYP/6-31+G(d,p) level based on the crystal structures obtained in this work. Orbital composition analysis was performed Hisnfeld method using the program Multiwfn 2.5.[8]

Syntheses of [(H_3ATSA)·H_2O] (1) and [(H_3ASA)·$4H_2O$] (2)

5-azotetrazolyl salicylic acid was synthesized according to the reported method in reference[9]: 5-amino-1H-tetrazole (2.06 g, 0.02 mol) was dissolved in 50 mL of distilled water, 3 mL of concentrated hydrochloric acid was added. The mix solution was stirred, cooled and kept at -5-0□ in an ice bath (ice and sodium chloride) and diazotized by slowly addition of a solution of sodium nitrite (0.02 mol, 1.38 g) in water (20 mL), followed by stirring for 30 min at -5-0□. Then a solution of salicylic acid (0.02 mol, 2.76 g) in enthanol (20 mL) was slowly added to the solution of the diazonium salt at 0-5□. The resulting mixture was stirred for 12 h and then the yellow precipitate was filtered and washed with water (yield: 73.2%). The yellow crystals of **1** and red crystals **2** were obtained after recrystallization in acid solution with pH about 5. FT-IR (KBr, cm^{-1}): 3241m, 1659s, 1494s, 1445s, 1186s, 760m, 696m for **1**. Anal. Calcd. for **1** of $C_8H_8N_6O_4$ (%): C, 38.07; H, 3.17; N, 33.31. Found(%): C, 38.11; H, 3.26; N, 33.35. FT-IR (KBr, cm^{-1}): 3456m, 3236s, 1661s, 1483s, 1444s, 1294s, 1156s, 891s, 756s, 695s, 533m for **2**. Anal. Calcd. for **2** of $C_8H_{14}N_6O_7$ (%): C, 31.35; H, 4.57; N, 27.43. Found(%): C, 31.25; H, 4.78; N, 27.38.

Syntheses of 3-6

10 mL aqueous solution of $MCl_3·6H_2O$ (0.01 mmol) was added to a solution of 5-azotetrazolyl salicylic acid (0.0504 g, 0.2 mmol) in 10mL of water and 10 mL of ethanol and stirred for 5 min and a drop of dilute $NH_3·H_2O$ (2 $mol·L^{-1}$) was added to adjust the pH to about 5. The resulting mixture was filtered and block crystals were obtained by slow evaporation of the filtrate after several days and washed with enthanol with yields of 36.5% for **3** (based on Dy^{3+}), 28.9% for **4** (based on Tb^{3+}), 28.5% for **5** (based on Gd^{3+}) and 33.2% for **6** (based on Sm^{3+}). Anal. Calcd. for **3** of $C_{32}H_{46}N_{24}O_{26}Dy_2$ (%): C, 25.47; H, 3.05; N, 22.28. Found(%): C, 25.49; H, 3.09; N, 22.32. FT-IR (KBr, cm^{-1}): 3196m, 1627m, 1580s, 1443s, 1175m, 837w, 683m, 563w. Anal. Calcd. for **4** of $C_{32}H_{46}N_{24}O_{26}Tb_2$ (%): C, 25.59; H, 3.07; N, 22.39. Found(%): C, 25.63; H, 3.13; N, 22.45. FT-IR (KBr, cm^{-1}): 3306m, 1635m, 1558s, 1391s, 1246m, 1149m, 756m, 671m. Anal. Calcd. for **5** of $C_{32}H_{42}N_{24}O_{26}Gd_2$ (%): C, 25.71; H, 2.81; N, 22.50. Found(%): C, 25.76; H, 2.84; N, 22.56. FT-IR (KBr, cm^{-1}): 3234m, 1628m, 1582s, 1387s, 1170m, 844w, 681m, 561w. Anal. Calcd. for **6** of $C_{32}H_{46}N_{24}O_{26}Sm_2$ (%): C, 25.88; H, 3.10; N, 22.65. Found(%): C, 25.60; H, 3.21; N, 22.69. FT-IR (KBr, cm^{-1}): 3151s, 1623m, 1593s, 1441s, 1173m, 840w, 684m.

Syntheses of 7

10 mL aqueous solution of $EuCl_3·6H_2O$ (0.0366 g, 0.01 mmol) was added to a solution of 5-azotetrazolyl salicylic acid (0.0756 g, 0.3 mmol) in 10 mL of water and 10 mL of ethanol and stirred for 5 min and a drop of dilute $NH_3·H_2O$ (2 $mol·L^{-1}$) was added to adjust the pH to about 5. The resulting mixture was filtered and block crystals were obtained by slow evaporation of the filtrate after several days and washed with enthanol. Yield: 31.6% (based on Eu^{3+}). Anal. Calcd. for **7** of $C_{64}H_{92}N_{48}O_{52}Eu_4$ (%): C, 25.83; H, 3.09; N, 22.60. Found(%): C, 25.86; H, 3.21; N, 22.65. FT-IR (KBr, cm^{-1}): 3396m, 3225m, 1627m, 1580s, 1441s, 1170s, 837m, 681m, 561m.

Results and discussion

Crystal structures of 1-7

Table 1 gives crystallographic data for compounds of **1**-**7**. The atomic labeling diagrams for **1** and **2** are shown in Fig. 1a, b, respectively. The crystals of **1** and **2** show yellow and red, respectively. **1** and **2** show two different space groups in which each unit cell contains a fundamental H_3ASA molecule and two different lattice water molecules. In **1** and **2**, the neutral H_3ASA molecules show a trans-enol-E isomer with the bond length for C2-O3 (phenol) being 1.354(3) Å for **1** and 1.341(4) Å for **2**. The dihedral angles between the tetrazole and phenyl ring of H_3ASA are 0.62º in **1** and 39.1º in **2**, which display a coplanar and a very twist structure, respectively. The yellow for **1** and red for **2** should originate from difference of dihedral angles. The O–H···O and O–H···N hydrogen bonding and π-π stacking interactions between tetrazole and phenyl rings are responsible for the stabilization of 3D supramolecular structure (Fig. S2, ESI†). The atomic labeling diagram of **3** is depicted in Fig. 1c and the atomic labeling diagrams of **4**-**7** see Fig. S3 ESI†. Complexes **3** and **4** are isostructural molecules in which each Dy^{3+} or Tb^{3+} ion coordinates to four carboxylate oxygen atoms from three ligands and four water molecules to give an eight-coordinated square antiprism. In complex **5**, each Gd^{3+} ion shows a square antiprism environment surrounded by eight oxygen atoms from four carboxylate oxygen atoms of three ligands and four water molecules. Each Sm^{3+} ion shows a distorted tricapped trigonal prismatic environment surrounded by nine oxygen atoms from four carboxylate oxygen atoms of three ligands and five water molecules in complex **6**. However, there are two μ_2 bridging water molecules in **6** (Fig. S3c, ESI†). In **7**, there are two different coordinating environment for Eu^{3+} ions in which an Eu^{3+} ion shows an eight-coordinated environment that is similar to Dy^{3+} ion in **3** and another Eu^{3+} ion is nine-coordinated with a tricapped trigonal prismatic structure. In **3**-**7**, the H_2ASA^- and $HASA^{2-}$ anions show trans-enol-E and trans-enol-Z isomers, respectively. The H_2ASA^- anion acts as a chelate ligand with two carboxylate oxygen atoms coordinating to a Ln^{3+} ion and each $HASA^{2-}$ anion acts as a μ_2 bridging ligand with two carboxylate oxygen atoms linking two Ln^{3+} ions to give a dinuclear complex. The $Ln^{3+}\cdots Ln^{3+}$ distances are 4.88, 4.85, 5.13, 4.23 and 4.93(5.32) Å for **3**-**7**, respectively. The H_2ASA^- and $HASA^{2-}$ anionic ligands are approximately coplanar because the dihedral angles between the tetrazole and phenyl ring are 1.30 and 7.62º for **3**, 1.53 and 7.88º for **4**, 1.35 and 3.62º for **5**, 10.30 and 11.20º for **6**, and 1.93 and 5.32º for **7**. In complexes of **3**-**7**, the π-π staking between tetrazole and phenyl aromatic rings and two O–H···O and O–H···N hydrogen bonding interactions link the complex units and lattice water molecules to give a 3D supramolecular packing structure (Fig. S4, ESI†).

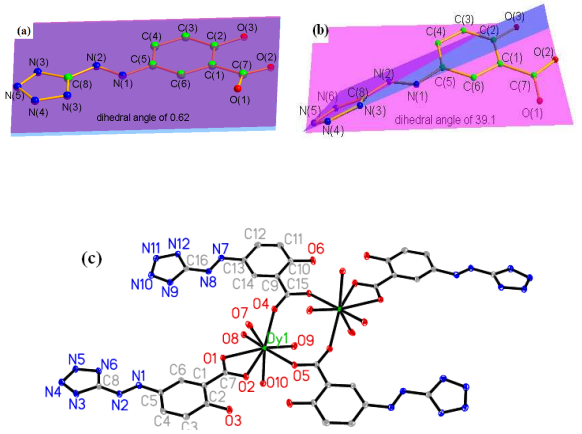

Fig. 1. The atomic labeling diagrams: (a) for **1**, (b) for **2**, (c) for **3**. All H atoms and lattice water molecules have been omitted for clarity.

The pH-dependent UV–vis spectra and photochromism of aqueous solution of 1

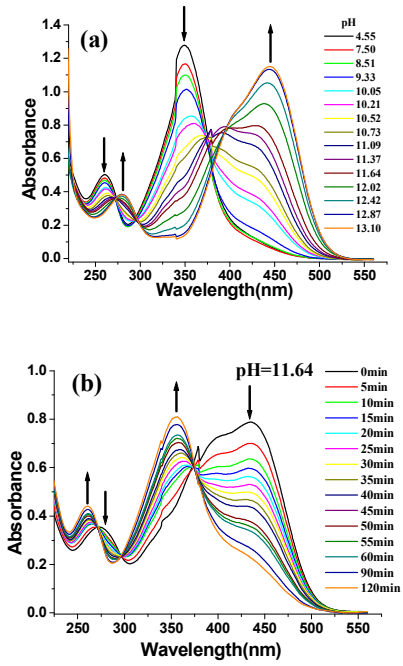

Fig. 2. (a) The pH-dependent UV-vis spectral changes of the aqueous solutions of **1**. (b)The UV-vis spectral changes of **1** in alkaline aqueous solution with pH of 11.64 under 365 nm UV irradiation.

Fig. 2a gives the pH-dependent UV–vis spectra of aqueous solution of **1** with concentration of 5×10^{-5} mol·dm^{-3}. The pH of the aqueous solution of **1** (5×10^{-5} mol·dm^{-3}) is 4.55. When the pH increases from 4.55 to 10.21 by titration with 2 mol·L^{-3} NaOH aqueous solution, the solutions show two clearly intense absorption peaks at 260 and 355 nm accompanied by a decrease in intensity and an unresolved weak shoulder peak around 430 nm. When the pH increases from 10.21 to 11.64, an added new red-shifted maximum absorption peak around 445 nm appears with an increase in intensity. When the pH increases from 11.64–13.10, the solution exhibits two maximum absorption peaks around 276 and 445 nm and a weak shoulder peak around 410 nm. The absorption peaks for aqueous solution of **1** in pH

scale of 4.55–13.10 should originate from the intrinsic chromophoric salicylic and tetrazolate π or azo n electronic excitation of trans-enol isomers of H_3ASA or its anions. Fig. 2b gives the photochromic properties for the alkaline aqueous solution of **1** with concentration of 5×10^{-5} mol·dm^{-3} and pH of 11.64 under 365 nm UV light irradiation at room temperature. Upon irradiation of the aqueous solution for 5 minutes with 365 nm UV light, two absorption peaks around 276 and 445 nm decrease in intensity and two new absorption peaks around 260 and 355 nm are noted and four regions with three isobestic points at 270, 297 and 375 nm can be distinguished. When the UV light irradiation continuously increases for 25 minutes, the absorption intensity at 355 nm peak largely increase. When the time of UV light irradiation increases for 60 minutes, the original two absorption peaks at 276 and 445 nm become unresolved. The phenomenon of maximum absorption peak transfer from 445 to 355 nm should originate from a trans-enol to cis–enol photoisomerization reaction of ASA^{3-} anion (scheme 1).[6c] Moreover, the photochromism of the aqueous solution of **1** is in accordance with the first-order kinetics (Fig. S5, ESI†), and the photochromism rate constant is about 2.824×10^{-2} min^{-1}.[6a] The temperature-dependent changes of UV-vis absorption spectra of alkaline aqueous solutions of **1** with concentration of 5×10^{-5} mol·dm^{-3} and pH of 11.64 in the temperature range of 32-100□ see Fig. S6, ESI†. When the temperature for aqueous solutions of **1** increases from 32 to 100□, three absorption peaks around 280, 400 and 445 nm decrease in intensity and two new absorption peaks around 260 and 355 nm are noted and four regions with three isobestic points at 270, 297 and 375 nm could be distinguished. The thermochromic properties for aqueous solutions of **1** are very similar with the characteristics of photochromism and should also be assigned to trans-enol to cis-enol isomeric reaction from ASA^{3-} anion. TD-DFT calculation for the absorption peaks of the alkaline aqueous solution of **1** and the photoisomerization reaction see the Electronic Supplementary Information (Fig. S7, ESI†).

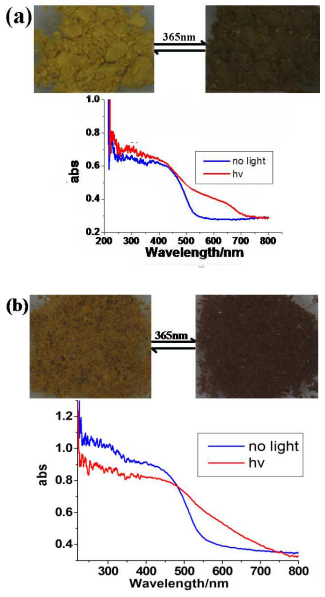

Fig. 3. (a), (b) The color and the corresponding to diffuse reflectance spectra for the crystal powder samples of **1** and **3** before and after 360nm UV light irradiation , respectively.

The photochromic properties for crystal powder samples of 1 and 3

Fig. 3 gives the color changes and the corresponding diffuse reflectance spectra for the crystal powder samples of **1** and **3** after 365 nm UV light irradiation at room temperature. From the diagrams, two crystal powder samples change to dark brown from original bright yellow for **1** and orange for **3** after irradiation for 30 min. Before light irradiation, the crystal powder samples of **1** and **3** display two distinguishable absorption peaks centered around 330 nm and 450 nm. After light irradiation, the samples show an a new red shift peak around 600 nm. The absorption peak around 330 nm and 450 nm can be attributed to the intrinsic π electronic transition from chromophoric tetrazolate, azo and salicylic groups. The larger red shift peak around 600 nm may be attributed to keto isomer from photo isomeric reaction.[10] The crystal powder samples of **4-7** show similar photochromic properties with **3** (Fig. S8, ESI†).

Luminescence for the solid samples of 1, 3-7

Photoluminescent spectra for the solid samples of **1**, **3-7** are depicted in Fig. 4 and Fig. S9, ESI†. Under 340 nm UV light excitation, the solid phase of **1** exhibit a maximum emissive peak around 460 nm and a shoulder peak around 370 nm (Fig. 4a). The solid sample of **1** show blue imaging observed by Fluorescent Microscope under UV light excitation (Fig. 4a insert). Both solid samples of **3** and **4** exhibit Dy^{3+} and Tb^{3+} ionic characteristic fluorescent emissive peaks under 340 nm UV light excitation, respectively (Fig. 4b). **3** exhibits 480 and 571 nm characteristic emissive peaks of Dy^{3+} ion and 457 and 529 nm characteristic peaks for H_2ASA^- and $HASA^{2-}$ anionic ligands. The 480 and 571 nm peaks should correspond to the $^4F_{9/2}$-$^6H_{15/2}$, $^4F_{9/2}$-$^6H_{13/2}$ transitions, respectively. The 457 and 529 nm maximum emissive peaks should originate from π electronic radiative relaxation of anionic ligands. **4** displays four characteristic emissive peaks of Tb^{3+} ion around 491, 543, 584 and 620 nm which correspond to the $^5D_4$-$^7F_6$, $^5D_4$-$^7F_5$, $^5D_4$-$^7F_4$, $^5D_4$-$^7F_3$ transitions, respectively. Two solid samples of **3** and **4** display the yellow-green imaging and green imaging taken by Fluorescent Microscope under UV light excitations, respectively (Fig. 4b, insert). However, the solid samples of **5-7** only display two fluorescent emissive peaks around 460 and 540 nm that come from anionic ligands and the characteristic fluorescent emissive peaks of Sm^{3+} and Eu^{3+} ions have not been observed (Fig. S9, ESI†). Based on the above photoluminescent spectra of **1**, **3-7**, a selective antenna effect of H_3ASA ligand for inducing Dy^{3+} and Tb^{3+} ion photoluminescence were found.

Magnetic properties of 3-7

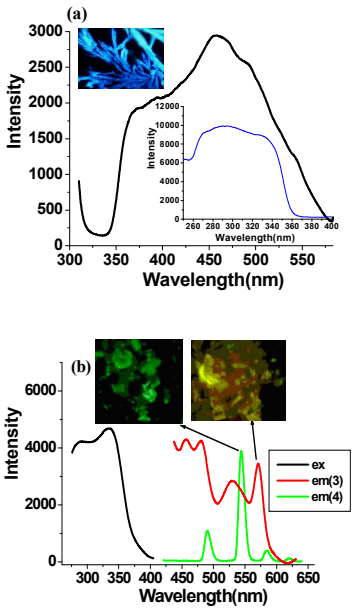

Fig. 4. (a) The emission spectra of **1**. (b) Excitation and emission spectra of **3** and **4**. Inset is the photoluminescent imaging of the solid sample of **1**, **3**, **4** taken Fluorescent Microscope.

In order to probe the magnetic behaviour of **3-7**, the temperature dependence of magnetic susceptibilities of **3-7** have been measured on microcrystalline samples over the temperature range 2−300 K under an applied direct current (dc) magnetic field of 1000 Oe. The plots of $\chi_M T$ versus T for **3-7**, where χ_M is the molar magnetic susceptibility, are shown in Fig. 5 and Fig. S10, ESI†. As shown in Fig. 5a, the observed $\chi_M T$ value for **3** at 300 K is 28.87 cm^3 K mol^{-1}, which is in agreement with the theoretical value of 28.34 cm^3 K mol^{-1} for two nonanteracting Dy^{3+} ions ($^6H_{15/2}$, S = 5/2, L = 5, g = 4/3, χT = 14.17 cm^3 K mol^{-1}). Upon decreasing the temperature, $\chi_M T$ gradually decreases to reach 23.40 cm^3 K mol^{-1} at 4.5 K. The decreasing values of $\chi_M T$ is most likely due to depopulation of the Stark sublevels in Dy^{3+} systems. Finally, below 4.5 K a sharp increase can be observed and the $\chi_M T$ reaches a maximum value of 25.60 cm^3 K mol^{-1} at 2 K. Such an increase can be attributed to intramolecular ferromagnetic interaction between the Dy^{3+} ions.[11,12] Magnetization (M) of **3** was collected from zero dc field to 40 kOe below 8 K are shown in the Fig. S11, ESI†. The magnetization of **3** shows a relatively rapid increase below 10 kOe and slow linear increase without completing saturation up to 40 kOe. The magnetization reaches a maximum value of 13.5 μ_B at 2.5 K and 40 kOe. This value is lower than the expected saturation value for two noninteracting Dy^{3+} ions [$g_J \times J = 4/3 \times 15/2 = 10$ μ_B per Dy^{3+}], which is likely due to crystal-field effects and the low-lying excited states. The M versus H/T plot is given in the insert of Fig. 5a. The lack of a superimposition on a single master curve as expected for an isotropic system with a well-defined ground state and the lower

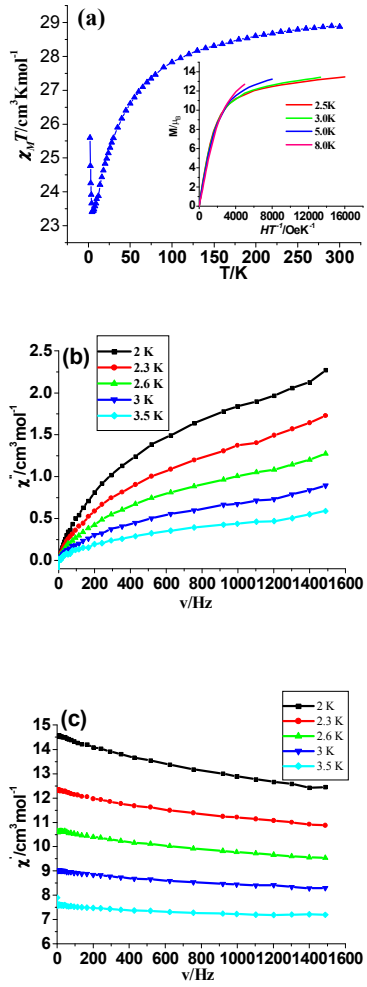

Fig. 5. (a) The plot of $\chi_M T$ versus T for **3** in the magnetic field of 1000 Oe in 2–300 K. Insert is the plot of M versus H/T in the field range 0–40000 Oe; (b) (c) frequency-dependence of the in-phase (χ') and out-of-phase (χ'') of ac susceptibility of **3** at 2 K-3.5 K.

magnetization values for **3** suggests the presence of low-lying excited states or/and significant magnetic anisotropy.[11] Alternating current (ac) magnetic susceptibility for **3** was performed in zero-dc field as a function of the ac frequence between 0.1 and 1500 Hz in the temperature range 2-3.5 K (Fig. 5b, c). The in-phase (χ') and out-of-phase (χ'') signals show obvious frequency dependence at low temperature, but no peak was observed (Fig. S12, ESI†). The energy barriers and relaxation times were approximated using a method recently employed by Bartolome et al.[13] based on the following equation:

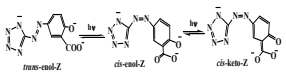

The calculated energy barrier of **3** was found to be 3.75 K whereas the relaxation time is 5.76×10^{-5} s (Fig. S13, ESI†).

This behavior is consistent with behavior as a single molecule magnet and the values of energy barrier and relaxation time are comparable with that observed in other Dy(III)-based SMMs.[12,14]

The plot $\chi_M T$ versus T for **4** is depicted in Fig. S10, ESI†. The $\chi_M T$ value of 24.09 cm^3 K mol^{-1} at 300 K is in good agreement with the expected value of 23.63 cm^3 K mol^{-1} for two noninteracting Tb^{3+} ions ($^7F_6$, S = 3, L = 3, g = 3/2). Upon cooling to 12K, $\chi_M T$ product gradually decreases to 21.47 cm^3 K mol^{-1}, which is most likely due to depopulation of the Stark sublevels in Tb^{3+} systems. Then $\chi_M T$ product increases to 27.85 cm^3 K mol^{-1} at 2 K, which is probably due to the presence of an intramolecular ferromagnetic interaction between the Tb^{3+} ions. The M versus H plot for **4** in the field range 0-70000 Oe below 8 K are shown in Fig. S14, ESI†. The magnetization measurement for **4** also shows a relatively rapid increase below 10 kOe and slow linear increase without completing saturation up to 70 kOe. The maximum magnetization of 11.5 μ_B at 70 kOe at 2.5 K is lower than the expected saturation value for two noninteracting Tb^{3+} ions [$g_J \times J = 3/2 \times 6 = 9$ μ_B per Tb^{3+}]. The M versus H/T plots for **4** shows no superimposition on a single master curve (Fig. S15, ESI†), which suggests the presence of low-lying excited states or/and significant magnetic anisotropy. The magnetic susceptibility studies of **5-7** were plotted as $\chi_M T$ versus T in Fig. S9, ESI†. The observed $\chi_M T$ values at 300 K are 12.27, 0.19 and 6.78 cm^3 K mol^{-1} for **5-7**, respectively. The theoretical calculated $\chi_M T$ values for two non-interacting Gd^{3+} ($^8S_{7/2}$, S=7/2, L=0, g=2) ions are 15.76cm^3 K mol^{-1}. Upon decreasing the temperature, $\chi_M T$ gradually decreases to reach 9.06 cm^3 K mol^{-1} at 2 K, which shows an antiferromagnetic interactions between Gd^{3+} ions. The $1/\chi_M$ versus T plot in the range from 300 to 2 K obeys the Curie-Weiss law ($\chi_M = C/(T - \theta)$) with a Weiss constant θ of -7.13 K (Fig. S16, ESI†). The negative Weiss constant further confirms an intramolecular antiferromagnetic interaction between adjacent Gd^{3+} ions. The field dependence of the magnetisation below 8 K reveals a relatively rapid increase of the magnetisation below 10 kOe and then a very slow linear increase without completing saturation up to 70 kOe (Fig. S17, ESI†). The maximum magnetization of 7.83 μ_B at 70 kOe is lower than the expected saturation value for two noninteracting Gd^{3+} ions [$g_J \times J = 2 \times 7/2 = 7$ μ_B per Gd^{3+}]. For **6**, the theoretical calculated $\chi_M T$ values for two non-interacting Sm^{3+} ($^6H_{5/2}$, S =5/2, L=5, g=2/7) ions are 0.18 cm^3 K mol^{-1}, which is in agreement with the observed value. However, the magnetic properties of Eu^{3+} ions in **7** are difficult to interpret even at room temperature due to the presence of thermally populated excited states.

Conclusions

In summary, a novel organic functional ligand of H_3ASA with two hydrated crystals with yellow (**1**) and red (**2**) and its five lanthanide complexes of **3-7** were first synthesized and reported. The solids of **1**, **3-7** display photochromic properties and the trans-enol to cis-enol transition for the ASA^{3-} anion is demonstrated by TD-DFT calculations. The photoluminescence for solids of **1**, **3-7** were reported and a selective antenna effect for H_3ASA ligand inducing Dy^{3+} and Tb^{3+} ionic photoluminescence were found. The magnetic properties for **3-7** were investigated and SMM behavior for **3** was demonstrated. This work demonstrates that H_3ASA based lanthanide complexes show photochromic, photoluminescent and magnetic properties and promise the novel functional materials that may be suitable for applications in optical and magnetic devices.

Acknowledgements

This work was supported by the National Natural Science Foundation of China (No. 21271052), Science and Technology Program Foundation of Guangzhou (No. 2013J4100016) and Program Foundation of the second batch of innovation teams of Guangzhou Bureau of Education (13C04).

Notes and references

[a]*School of Chemistry and Chemical Engineering, Guangzhou Key Laboratory for Environmentally Functional Materials and Technology, Guangzhou University, Guangzhou, 510006, China, E-mail: dw320@aliyun.com.*
[b]*Department of Chemistry, Tianjin Normal University, Tianjin, 300383, China, E-mail: hxxysyq@mal.tjnu.edu.cn*

† Footnotes should appear here. These might include comments relevant to but not central to the matter under discussion, limited experimental and spectral data, and crystallographic data.

Electronic Supplementary Information (ESI) available: The atomic labeling diagrams of **4-7**; 3D supramolecular structure of **1-7**; Photoisomerization of **1;** The temperature-dependent changes of UV-vis absorption spectra of aqueous solutions of **1**; TD-DFT calculations for the absorption spectra of the alkaline aqueous solution of **1**; The color changes of **4-7** before and after 365 nm UV irradiation; Luminescent spectra of **1** and **5-7**; X-ray powder diffraction patterns for **3-7;** The plot of $\chi_M T$ versus T for **4-7**; M versus H plots in the field range 0-40000(70000) Oe for **3-5**; M versus H/T plots in the field range 0–70000 Oe for **4**; Temperature-dependence of the in-phase (χ') and out-of-phase (χ'') of ac susceptibility of **3** at 250-1500 Hz; The $1/\chi_M$ versus T plot in the range from 300 to 2 K for **5** and CIF files. See DOI: 10.1039/b000000x/

1 (a) J. Feng and H. J. Zhang, *Chem. Soc. Rev.*, 2013, **42**, 387; (b) Y. Cui, Y. Yue, G. Qian and B. *Chen, Chem. Rev.*, 2012, **112**, 1126; (c) L. D. Carlos, R. A. S. Ferreira, V. Z. Bermudez, B. Julián-López and P. Escribano, *Chem. Soc. Rev.*, 2011, **40**, 536; (d) A. Dolbecq, E. Dumas, C. R. Mayer and P. Mialane, *Chem. Rev.*, 2010, **110**, 6009; (e)C. Sanchez, B. Julian, P. Belleville and M. Popall, *J. Mater. Chem.*, 2005, **15**, 3559; (f) K. Binnemans, *Chem. Rev.*, 2009, **109**, 4283; (g) Z. H. Zhang, T. -a. Okamura, Y. Hasegawa, H. Kawaguchi, L. Y. Kong, W. Y. Sun and N. Ueyama, *Inorg. Chem.*, 2005, **44**, 6219.

2 (a) E. DeOliveira, C. R. Neri, O. A. Serra and A. G. S. Prado, *Chem. Mater.*, 2007, **19**, 5437; (b) J. D. Rinehart, M. Fang, W. J. Evans and J. R. Long, *Nat. Chem.*, 2011, **3**, 538; (c) H. B. Kagan, *Chem. Rev.*, 2002, **102**, 1805; (d) R. Sessoli and A. K. Powell, *Coord. Chem. Rev.*, 2009, **253**, 2328; (e) S. V. Eliseeva and J.-C. G. Bünzli, *Chem. Soc. Rev.*, 2010, **39**, 189; (f) J. Rocha, L. D. Carlos, F. A. A. Paz and D. Ananias, *Chem. Soc. Rev.*, 2011, **40**, 926.

3 (a) P. Lodahl, A. V. Driel, I. Nikolaev, A. Irman, K. Overgaag, D. Vanmaekelbergh, W. Vos, *Nature*, 2004, **430**, 654; (b) X.-Y. Chen, G. S. Goff, W. C. Ewing, B. L. Scott and W. Runde, *Inorg. Chem.*, 2012, **51**, 13254; (c) G. Wang, Q. Peng and Y. Li, *Acc. Chem. Res.*, 2011, **44**, 322; (d) A. de Bettencourt-Dias, P. S. Barber and Bauer S. *J. Am. Chem. Soc.*, 2012, **134**, 6987; (e) E. Pershagen, J. Nordholm and K. E. Borbas, *J. Am. Chem. Soc.*, 2012, **134** , 9832; (f) P. P. Lima, M. M. Nolasco, F. A. A. Paz, R. A. S. Ferreira, R. L. Longo, O. L. Malta and L. D. Carlos, *Chem. Mater.*, 2013, **25**, 586.

4 (a) I. P. Pozdnyakova, A. Pigliucci, N. Tkachenko, V. F. Plyusnin, E. Vauthey and H. Lemmetyinen, *J. Phys. Org. Chem.*, 2009, **22**, 449; (b) H.-C. Lüdemann, F. Hillenkamp and R. W. Redmond, *J. Phys. Chem. A*, 2000, **104**, 3884; (c) N. Matyasovszky, M. Tian and A. C. Chen, *J. Phys. Chem. A*, 2009, **113**, 9348; (d) G. Aromi, L. A. Barrios, O. Roubeau and P. Gamez, *Coord. Chem. Rev.*, 2011, **255**, 485; (e) J.-P. Zhang, Y.-B. Zhang, J.-B. Lin and X.-M. Chen, *Chem. Rev.*, 2012, **112**, 1001.

5 (a) M. P. Placidi, A. J. L. Villaraza, L. S. Natrajan, D. Sykes, A. M. Kenwright and S. Faulkner, *J. Am. Chem. Soc.*, 2009, **131**, 9916; (b) H. Nishihara, *Coord. Chem. Rev.*, 2005, **249**, 1468.

6 (a) Y.-C. Li, C. Qi, S.-H. Li, H.-J. Zhang, C.-H. Sun, Y.-Z. Yu and S.-P. Pang, *J. Am. Chem. Soc.*, 2010, **132**, 12172; (b) T. M. Klapötke and D. G. Piercey, *Inorg. Chem.*, 2011, **50**, 2732; (c) J.-M. Lin, W.-B. Chen, X.-M. Lin, A.-H. Lin, C.-Y. Ma, W. Dong and C.-E. Tian, *Chem. Commun*., 2011, **47**, 2402.

7 J.-M. Lin, M. Yang, Y.-X. Qiu, W.-B. Chen, H. Yan, F.-X. Gao, Z.-J. OuYang, W. Dong and T.-C. Kuang, *ChemPlusChem*, 2013, **78**, 598.

8 T. Lu and F. Chen, *J. Comp. Chem.*, 2012, **33**, 580, http://Multiwfn.codeplex.com.

9 I. L. Shegal, K. V. Stanovkina, N. G. Kovalenko and L. M. Shegal, *Khim. Geterotsikl. Soedin*, 1974, **3**, 422.

10 M. L. Kahn, J.-P. Sutter, S. Golhen, P. Guionneau, L. Ouahab, O. Kahn and D. Chasseau, *J. Am. Chem. Soc.*, 2000, **122**, 3413.

11 (a) L. Sorace, C. Benelli and D. Gatteschi, *Chem. Soc. Rev.*, 2011, **40**, 3092; (b) Y.-N. Guo, X.-H. Chen, S. Xue and J.-K. Tang, *Inorg. Chem.*, 2011, **50**, 9705; (c) V. Chandrasekhar, P. Bag, M. Speldrich, J. V. Leusen and P. Kögerler, *Inorg. Chem.*, 2013, **52**, 5035; (d) G. F. Xu, Q. L. Wang, P. Gamez, Y. Ma, R. Cle ´ rac, J. k. Tang, S. P. Yan, P. Cheng and D. Z. Liao, *Chem. Commun.*, 2010, **46**, 1506; (e) M. A. AlDamen, S. Cardona-Serra, J. M. Clemente-Juan, E. Coronado, A. Gaita-Ariño, C. Martí-Gastaldo, F. Luis and O. Montero, *Inorg. Chem.*, 2009, **48**, 3467.

12 (a) P.-H. Lin, T. J. Burchell, R. Clerac and M. Murugesu, *Angew. Chem., Int. Ed.*, 2008, **47**, 8848; (b) P.-H. Lin, W.-B. Sun, M.-F. Yu, G.-M. Li, P.-F. Yan and M. Murugesu, *Chem. Commun.*, 2011, **47**, 10993.

13 J. Bartolome, G. Filoti, V. Kuncser, G. Schinteie, V. Mereacre, C. E. Anson, A. K. Powell, D. Prodius and C. Turta, *Phys. Rev. B*, 2009, **80**, 014430.

14 (a) M. R. Saber and K. R. Dunbar, *Chem. Commun.,* 2014, **50**, 2177; (b) Y.-M. Song, F. Luo, M.-B. Luo, Z.-W. Liao, G.-M. Sun, X.-Z. Tian, Y. Zhu, Z.-J. Yuan, S.-J. Liu, W.-Y. Xu and X.-F. Feng, *Chem. Commun.*, 2012, **48**, 1006; (c) D.-P. Li, X.-P. Zhang, T.-W. Wang, B.-B. Ma, C.-H. Li, Y.-Z. Li and X.-Z. You, *Chem. Commun.*, 2011, **47**, 6867; (d) H. Wang, C. Liu, T. Liu, S. Zeng, W. Cao, Q. Ma,C. Duan, J. Dou and J. Jiang, *Dalton Trans.*, 2013, **42**, 15355; (e) R. J. Blagg, C. A. Muryn, E. J. L. McInnes, F. Tuna and R. E. P. Winpenny, *Angew. Chem. Int. Ed.*, 2011, **50**, 6530; (f) S.-D. Jiang, B.-W. Wang, G. Su, Z.-M. Wang,and S. Gao, *Angew. Chem.*, 2010, **122**, 7610; (g) R. A. Layfield, J. J. W. McDouall, S.A. Sulway, F. Tuna, D. Collison and R. E. P. Winpenny, *Chem. Eur. J.*, 2010, **16**, 4442.

Journal Name RSCPublishing

ARTICLE

Table 1 The crystal data and data collection parameters for **1**–**7**.

	1	**2**	**3**	**4**	**5**	**6**	**7**
formula	$C_8H_8N_6O_4$	$C_8H_{14}N_6O_7$	$C_{32}H_{46}Dy_2N_{24}O_{26}$	$C_{32}H_{46}N_{24}O_{26}Tb_2$	$C_{32}H_{46}Gd_2N_{24}O_{26}$	$C_{32}H_{46}N_{24}O_{26}Sm_2$	$C_{64}H_{92}Eu_4N_{48}O_{52}$
Formula weight	252.20	306.25	1507.93	1500.79	1497.43	1483.65	2973.74
Crystal system	monoclinic	monoclinic	triclinic	triclinic	triclinic	triclinic	triclinic
Space group	$P2_1/n$	C2/c	Pī	Pī	Pī	Pī	Pī
a/Å	3.9726(2)	27.104(10)	9.6459(14)	9.6491(13)	9.76740(10)	9.6865(12)	11.8805(2)
b/Å	10.6370(6)	3.8044(13)	11.9523(18)	11.9680(17)	11.8082(2)	11.7997(14)	14.6591(3)
c/Å	24.5982(13)	27.047(9)	12.8750(19)	12.9137(18)	12.5681(2)	13.1112(16)	16.4889(3)
α/°	90.00	90.00	110.424(2)	110.617(2)	109.4910(10)	111.997(2)	99.9840(10)
β/°	91.158(4)	101.58(2)	94.582(2)	94.603(2)	94.4350(10)	95.839(2)	95.9560(10)
γ/°	90.00	90.00	105.450(2)	105.596(2)	104.6290(10)	104.792(2)	110.3260(10)
Volume/$Å^3$	1039.22(10)	2732.2(17)	1316.0(3)	1318.8(3)	1301.27(4)	1310.5(3)	2609.93(9)
Z	4	8	1	1	1	1	1
ρ_{calc}mg/mm^3	1.612	1.489	1.903	1.890	1.911	1.880	1.892
m/mm^{-1}	0.133	0.131	2.926	2.769	2.637	2.328	2.491
F(000)	520.0	1280.0	746.0	744.0	742.0	738.0	1480.0
Reflections collected	6711	10622	11004	11019	19222	10980	41058
Independent reflections	1835[R(int) = 0.0318]	3135[R(int) = 0.0454]	5800[R(int) = 0.0186]	5783[R(int) = 0.0166]	5122[R(int) = 0.0255]	5770[R(int) = 0.0182]	12090[R(int) = 0.0212]
Goodness-of-fit on F^2	1.090	1.075	1.092	1.157	1.039	1.194	1.036
Final R indexes [I>=2σ (I)]	R_1 = 0.0561, wR_2 = 0.1563	R_1 = 0.0705, wR_2 = 0.2087	R_1 = 0.0236, wR_2 = 0.0538	R_1 = 0.0211, wR_2 = 0.0567	R_1 = 0.0322, wR_2 = 0.0721	R_1 = 0.0236, wR_2 = 0.0667	R_1 = 0.0244, wR_2 = 0.0594
Final R indexes [all data]	R_1 = 0.0710, wR_2 = 0.1663	R_1 = 0.1192, wR_2 = 0.2402	R_1 = 0.0291, wR_2 = 0.0568	R_1 = 0.0238, wR_2 = 0.0609	R_1 = 0.0367, wR_2 = 0.0784	R_1 = 0.0282, wR_2 = 0.0748	R_1 = 0.0292, wR_2 = 0.0621

$^aR = \sum||F_o|-|F_c||/\sum|F_o|$. $^bwR_2 = [\sum w(F_o^2 - F_c^2)^2/\sum w(F_o^2)^2]^{1/2}$